

Prospects for detection rate of very-high-energy γ -ray emissions from short γ -ray bursts with the HADAR experiment

QI-LING CHEN,¹ PEI-JIN HU,¹ JING-JING SU,¹ MING-MING KANG,¹ YI-QING GUO,^{2,3} TIAN-LU CHEN,⁴
DAN-ZENG LUO-BU,⁴ YU-FAN FAN,⁴ YOU-LIANG FENG,⁴ QI GAO,⁴ QUAN-BU GOU,² HONG-BO HU,^{2,3} HAI-JIN LI,⁴
CHENG LIU,² MAO-YUAN LIU,⁴ WEI LIU,² XIANG-LI QIAN,^{5,4} BING-QIANG QIAO,² HUI-YING SUN,⁵ XU WANG,⁵
ZHEN WANG,⁶ GUANG-GUANG XIN,⁷ YU-HUA YAO,⁸ QIANG YUAN,⁹ YI ZHANG,⁹ AND BING ZHAO²

¹College of Physics, Sichuan University, Chengdu 610064, China

²Key Laboratory of Particle Astrophysics, Institute of High Energy Physics, Chinese Academy of Sciences, Beijing 100049, China

³University of Chinese Academy of Sciences, 19 A Yuquan Rd, Shijingshan District, Beijing 100049, China

⁴The Key Laboratory of Cosmic Rays (Tibet University), Ministry of Education, Lhasa 850000, China

⁵School of Intelligent Engineering, Shandong Management University, Jinan 250357, China

⁶Tsung-Dao Lee Institute, Shanghai Jiao Tong University, Shanghai 200240, China

⁷School of Physics and Technology, Wuhan University, Wuhan 430072, China

⁸College of Physics, Chongqing University, Chongqing 401331, China

⁹Key Laboratory of Dark Matter and Space Astronomy, Purple Mountain Observatory, Chinese Academy of Sciences, Nanjing 210008, China

ABSTRACT

The observation of short gamma ray bursts (SGRBs) in the TeV energy range plays an important role in understanding the radiation mechanism and probing new areas of physics such as Lorentz invariance violation. However, no SGRB has been observed in this energy range due to the short duration of SGRBs and the weakness of current experiments. New experiments with new technology are required to detect sub-TeV SGRBs. In this work, we observe the very high energy (VHE) γ -ray emissions from SGRBs and calculate the annual detection rate with the High Altitude Detection of Astronomical Radiation HADAR (HADAR) experiment. First, a set of pseudo-SGRB samples is generated and checked using the observations of Fermi-GBM, Fermi-LAT, and SWIFT measurements. The annual detection rate is calculated from these SGRB samples based on the performance of the HADAR instrument. As a result, the HADAR experiment can detect 0.5 SGRB per year if the spectral break-off of γ -rays caused by the internal absorption is larger than 100 GeV. For a GRB09010-like GRB in HADAR's view, it should be possible to detect approximately 2000 photons considering the internal absorption. With a time delay assumption due to the Lorentz invariance violation effects, a simulated light curve of GRB090510 has evident energy dependence. We hope that the HADAR experiment can perform the SGRB observations and test our calculations in the future.

1. INTRODUCTION

GRBs are some of the most powerful explosions in the universe and can last from 10 ms to several hours as prompt emissions, releasing most of the energy in the form of photons from 30 keV to a few MeV. The properties of GRBs mainly include two components of temporal and spectral information. First, from the point view of the temporal property, its prompt phase has a bimodal duration distribution separated at $t \sim 2$ s, indicating that there are two different groups as the long GRBs (LGRBs) with $t_{LGRB} > 2$ s and SGRBs with $t_{SGRB} < 2$ s (Kouveliotou et al. 1993; Meszaros 2006).

LGRBs are likely formed by the collapses of massive star cores (Woosley 1993; MacFadyen & Woosley 1999), while SGRBs are thought to come from the coalescence of compact binary systems, such as binary neutron stars (BNS) and neutron star-black hole (NS-BH) systems (Blinnikov et al. 1984; Paczynski 1986; Eichler et al. 1989). The associated events GW170817/GRB170817A (Abbott et al. 2017) from a BNS merger make the grounded assumption that BNS mergers are sources (or parts of the sources) of SGRBs. For a spectrum, a two-component structure has been revealed above tens of MeV. At low energy, an exponential Band-function can describe observations well (Band et al. 1993; Band 2003), which is possibly induced by the synchrotron radiation process (Oganesyan et al. 2017, 2018, 2019; Ravasio et al. 2018). At high energy, the model predicts

that another component generated from the inverse-Compton (IC) process should exist (Mészáros & Rees 1994; Dermer et al. 2000; Sari & Esin 2001; Zhang & Mészáros 2001). In the past few decades, great achievements have been made in experimental measurements to study temporal and spectral characteristics. It is evident that the measurements are relatively rich at low energy, but observations in the TeV band are more desirable.

The milestone progress was achieved in observations of γ -ray emissions in the TeV band in recent years. The MAGIC (Major Atmospheric Gamma Imaging Cherenkov) and H.E.S.S. (High Energy Stereoscopic System) experiments discovered sub-TeV γ -ray emissions in GRB190114C and GRB180720B (Veres et al. 2019; Abdalla et al. 2019). Following these observations, the HESS experiments detected photons with energies of up to 4 TeV from GRB190829A, between 4 and 56 hr after the trigger time (collaboration et al. 2021). The brightest GRB221009A was observed in a multi-band just recently. It is very exciting that the highest photons can reach 18 TeV (Huang et al. 2022). This new discovery opened the observation window of γ -ray emissions of GRBs in the TeV band and confirmed the new radiation mechanism expected by the model, named the IC process (Mészáros & Rees 1994; Dermer et al. 2000; Sari & Esin 2001; Zhang & Mészáros 2001). Those discoveries shined a new light on the central engine and radiation mechanism and probed new physics such as LIV and Dark Matter (DM) (Amelino-Camelia et al. 1998; Nakagawa et al. 2023; González et al. 2023). It is unfortunate that the γ -ray emissions at TeV energy were only observed at the afterglow phase of LGRBs. No prompt emission has yet been observed for GRBs at this energy band, let alone SGRBs. Despite this, TeV γ -ray emissions from SGRBs can play very important roles in understanding LIV because of the short duration of SGRBs. Therefore, scientists are looking forward to the γ -ray observation results in the TeV energy region.

Space-borne and ground-based experiments have both contributed to the study of LIV. GRB090510 is a typical bright SGRB among high-energy observations, with a photon observed at 31 GeV arriving at 0.829 s after the trigger of Fermi-GBM. This SGRB provides conditions to constrain the LIV effect and provides a lower limit for the linear modification of the photon dispersion relationship, which is $E_{QG,1} > 1.49 \times 10^{19}$ GeV (Abdo et al. 2009), which is the best down-limit. However, only one photon is detected above 10 GeV by Fermi-LAT in this work (Abdo et al. 2009), and the event number with high statistics is better for confirmation of this important result. The shortage of space-borne experiments includes a limited effective area of ~ 1 m², which leads to in-

sufficient sensitivity in the high-energy range. Imaging atmospheric Cherenkov telescopes (IACT) experiments have high sensitivity above 100 GeV energy, but the fatal weakness for SGRBs is their field of view (FOV) with a value of only several degrees (Bolmont et al. 2014; Aleksić et al. 2016; leeds. ac. uk <http://www.cta-observatory.org> et al. 2011). However, the Cherenkov Telescope Array (CTA) will detect prompt emissions of SGRBs when they are slewed to the source before the BNS mergers (Banerjee et al. 2022). The traditional arrays of CRs, such as HAWC (High-Altitude Water Cherenkov) and LHAASO (Large High Altitude Air Shower Observatory), have good performance above TeV energy and wide FOV, but these arrays cannot be compared with IACT detectors at the 100 GeV energy range. The optimal choice is an IACT with a wide FOV such as the HADAR project. Therefore, it is necessary to know the detection capability of SGRBs for the HADAR experiment. In this work, the annual detection rate based on a set of pseudo-SGRB samples is generated and checked with the observations of space-borne experiments.

Our work in this paper is organized as follows. First, we provide a brief introduction to the HADAR experiment and its performance parameters in section 2. Then, to predict the detection rate of SGRBs with HADAR as reliably as possible, we model the pseudo-SGRBs and the simulations of the detecting process with consideration of the performance of detectors for both Fermi-GBM (for consistency check) and HADAR. The simulation methods and results are shown in Sections 3 and 4, respectively. In Section 4, we also describe the simulation of the observational results of GRB090510 in HADAR's case, given as a light curve with consideration of LIV effects. In Section 5, we describe the conclusion of our findings.

2. HADAR EXPERIMENT

The HADAR project is proposed for construction in YangBaJing, Tibet of China at the altitude of 4300 m. As shown in Figure 1, this project has a hybrid array, which includes the two parts of the water lens and traditional scintillators.

The water lens array is composed of four of the same telescopes with a diameter of 5 m and a distance of 100 m between two telescopes. The right panel of the figure 1 presents the detailed profile structure of a single water lens. The profile structure mainly consists of an acrylic spherical cap lens with a diameter of 5 m, a cylindrical tank with a radius of 4 m and a height of 7 m, and a camera with an array of 18,961 Photomultiplier tubes (PMTs) at each 5 cm in diameter. The steel tank,

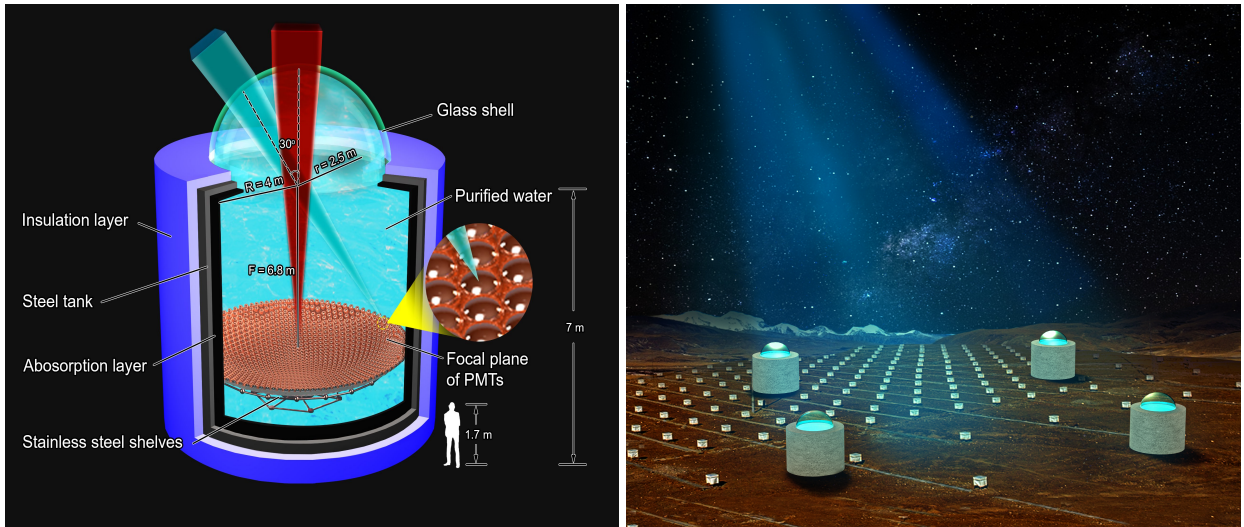


Fig. 1. The HADAR project. Left: Layout of the HADAR array with a water lens. Right: Profile design of each telescope.

which contains an absorption layer in the inside wall and a thermal insulation material coating on the outer wall, is filled with purified water to reflect radiation emissions to the PMTs. The PMTs are placed in the focal plane of the lens and arranged as a series of concentric ring matrixes supported by a stainless-steel space frame. The water lens array is designed to focus on the transient sources, such as GRBs, and AGNs (active galactic nuclei), in the northern sky to measure primary γ -rays in the energy range from 10 GeV to 100 TeV. Thanks to the properties of the water lens, it has an FOV of 0.84 sr (30° zenith angle), which is almost one order of magnitude larger than that of IACTs such as H.E.S.S., MAGIC, and CTA (Bolmont et al. 2014; Aleksić et al. 2016; leeds. ac. uk <http://www.cta-observatory.org> et al. 2011). It is more important that the effective area, angular resolution, and energy resolution at 300 GeV energy can reach 10000 m^2 , 0.5° , and 20%, respectively, which is comparable to H.E.S.S. and MAGIC, except for the angular resolution. The water lens detection design can meet the observation requirements of our physical targets.

The scintillator array is composed of 100 detectors and is designed to perform joint observations with a water lens. The installation and maintenance of a scintillator detector are particularly simple, and a scintillator detector can achieve a long-term stable performance as well as a good time resolution, which is widely used in extensive air shower (EAS) arrays (collaboration et al. 2010). The frame structure is made of stainless steel with an upside-down pyramidal shape, called a box of light guide (BLG). The interfaces of a BLG are light-tight, with a reflective material, Dupont Tyvek covering the inner surface with the purpose of increasing the effi-

ciency of light collection significantly. A KD2000 plastic scintillator is adopted with dimensions of $1 \text{ m} \times 1 \text{ m} \times 2 \text{ cm}$ and placed onto the top of the frame. A PMT with a diameter of 2 inches is chosen and installed on the bottom. When charged particles induced by the primary CRs pass through the scintillator, photons are generated. Some of these photons can be refracted several times in BLG, and some of them finally can reach and be collected by the PMT. The main function of a scintillator detector is to measure the coincidence with the water lens and to confirm the performance of the water lens.

3. MODELING SGRB SAMPLES

To estimate the detection rate of the prompt emissions from SGRBs for HADAR, we adopt a simulation method based on Monte Carlo. A set of SGRB samples is generated according to the phenomenological models of their intrinsic parameters, such as space density, luminosity, energy spectrum, temporal duration, and EBL attenuation. The expected detection rate is calculated using the spectra for each GRB and the HADAR sensitivity.

3.1. Redshift Distribution

The redshift distribution describes the number of SGRBs per unit redshift bin dz per unit (observed) time dt , which is written as (Zhang 2018):

$$\frac{dN}{dt dz} = \frac{\dot{\rho}(z)}{1+z} \frac{dV(z)}{dz}, \quad (1)$$

where

$$\frac{dV(z)}{dz} = \frac{c}{H_0} \frac{4\pi D_L^2}{(1+z)^2 [\Omega_m (1+z)^3 + \Omega_\Lambda]^{1/2}}. \quad (2)$$

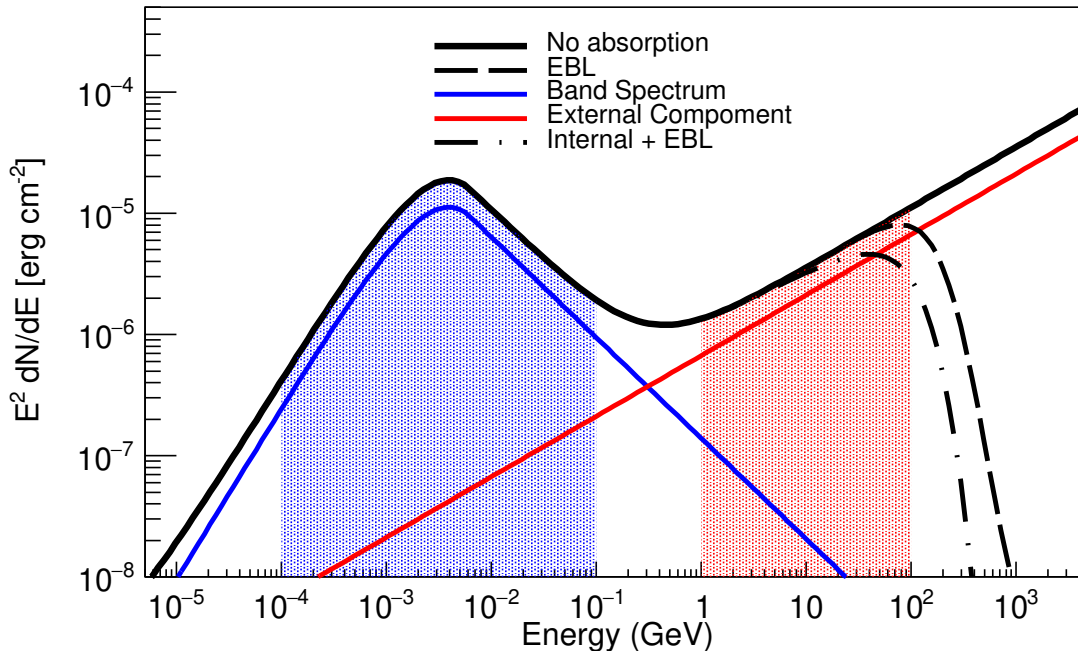


Fig. 2. The energy spectrum of the Band function with EBL and internal absorption is considered. The blue and red solid lines represent the spectra of the Band function and the extra component, respectively. The dashed and dotted lines represent the spectra when taking the EBL absorption of Ref. (Finke et al. 2010) and the internal + EBL absorption into account, respectively. The redshift is adopted as $z = 0.903$, and the cutoff energy is 50 GeV. The values of β_{ext} and R_{ext} are -1.5 and 0.1, respectively. R_{ext} represents the ratio of the fluences in the energy range of 100 MeV to 100 GeV to 100 keV to 100 MeV, which are the red-banded and blue-shaded regions, respectively. To distinguish the individual components of the emission from the total combined flux, both the Band spectrum and the extra component are scaled by 0.5.

In our work, we adopt $H_0 = 67.4 \text{ km s}^{-1} \text{ Mpc}$, $\Omega_m = 0.315$, and $\Omega_\Lambda = 0.685$ (Group 2020). In addition, $\dot{\rho}(z)$ is the event rate density at z (in units of $\text{Gpc}^{-3} \text{ yr}^{-1}$), which is (Howell et al. 2019; Regimbau & Hughes 2009):

$$\dot{\rho}(z) \propto (1+z) \int_{t_{min}}^{t_{max}} R_F(z_f) P(t_d) dt_d, \quad (3)$$

where $P(t_d) \propto 1/t_d$, $t_{min} = 20 \text{ Myr}$ is the minimum delay time for a BNS system to evolve to merge, and t_{max} is the age of the universe at the time of merging $t(z)$. $R_F(z_f)$ is the star formation history (SFH), which is adopted from Ref. (Madau & Dickinson 2014). We normalize the event rate density $\dot{\rho}(z)$ with $1540_{-1220}^{+3200} \text{ Gpc}^{-3} \text{ yr}^{-1}$ (Abbott et al. 2017), which corresponds to the local event rate density at $z = 0$.

The delay time t_d between the formation of the binary system $t_f(z_f)$ and the age of the universe at the time of merger $t(z)$ is given as

$$t_d = \int_z^{z_f} \frac{dz'}{H_0(1+z')[\Omega_m(1+z')^3 + \Omega_\Lambda]^{1/2}}, \quad (4)$$

where z_f and z represent the redshifts at which the BNS systems form and merge, respectively.

3.2. Luminosity Function

We explore the expression of the SGRB's luminosity function in a broken power law, which is widely adopted in other works:

$$\Phi(L) = A \begin{cases} (\frac{L}{L_c})^\alpha, & L \leq L_c \\ (\frac{L}{L_c})^\beta, & L > L_c \end{cases} \quad (5)$$

A is the normalization constant, L_c is the break luminosity, and α and β are the power-law indices. In this research, we adopt $\alpha = -1.95$, $\beta = -3$, $L_c = 2 \times 10^{52} \text{ erg s}^{-1}$, $L_{min} = 1 \times 10^{49} \text{ erg s}^{-1}$ (Wanderman & Piran 2015).

3.3. Prompt Emission Spectrum

The prompt emission spectrum of GRBs may include two spectral components: a non-thermal Band component (Band) and a non-thermal power law component extending to high energies (PL). In this work, we assume all of the pseudo-SGRBs have the Band + PL spectrum.

The Band function is usually used to fit the spectrum of a GRB when the detector's energy band is wide enough. The Band function is (Band et al. 1993; Band

2003):

$$N(E) = A_0 \begin{cases} \left(\frac{E}{E_0}\right)^\alpha \exp(-E/E_p), & E \leq E_c \\ \left(\frac{E_c}{E_0}\right)^{\alpha-\beta} \exp(\beta - \alpha) \left(\frac{E}{E_0}\right)^\beta, & E > E_c \end{cases} \quad (6)$$

where $E_0 = 100$ keV and $E_c = (\alpha - \beta)E_p$. A_0 is the normalization constant in units of photons $\text{s}^{-1} \text{cm}^{-1} \text{keV}^{-1}$. α and β are the low and high energy photon indices, respectively, and E_p is the peak energy of the spectrum. In this work, α and β are adopted from the observations of Fermi-GBM (Poolakkil et al. 2021). E_p is determined by the $E_p - L_p$ relationships examined by Ref. (Tsutsui et al. 2013).

Beyond the Band function, a high-energy and power law spectral component is necessary to fit the spectrum in some GRBs (Abdo et al. 2009; Ackermann et al. 2010, 2011). The power law component is the dominant contribution to the high-energy prompt emission beyond tens of GeV. In this work, we introduce the extra component for GRB spectra. The luminosity ratio $R_{ext} = L_{ext}/L_{ave}$ and spectral index β_{ext} are used to describe the extra component. L_{ext} is the luminosity of the extra component and L_{ave} is the luminosity of the Band component. We take $R_{ext} = 0.1$, $\beta_{ext} = 1.5$.

3.4. $\gamma\gamma$ Absorption

The photons with the highest energies within the emission region may be strongly attenuated by the low-energy photons through the $\gamma\gamma \rightarrow e^\pm$ interaction. The specific spectral breaks occur because of the two-photon pair production, which is related to different bulk Lorentz factors and the fireball radius (Chen et al. 2018; Asano & Inoue 2007). In this work, we introduce an exponential cutoff on the spectrum to describe the internal absorption when calculating the detection rate. For typical burst parameters, the internal shock spectrum cuts off above a threshold energy of $E_{\gamma,th} \sim 10 - 100$ GeV and has no internal cutoff with a large enough bulk Lorentz factor (Razzaque et al. 2004), so the cases of 30 GeV, 50 GeV, 100 GeV, and 1 TeV with and without an energy cutoff are considered.

High-energy photons from distant astrophysical sources are subject to attenuation because of the two-photon pair production with the EBL. This absorption of γ -rays can be described as $e^{-\tau(E,z)}$, where $\tau(E,z)$ is the optical depth for the γ -rays at energy E . The EBL attenuation introduced in the work of Ref. (Finke et al. 2010) is used by default. Figure 2 shows the energy spectrum of the SGRBs. The EBL and internal absorption are considered.

3.5. Temporal Properties

The duration of the GRBs is approximately estimated using T_{90} , which corresponds to the time in which 90% of the counts arrive. T_{90} is described as (Ghisellini et al. 2010; Kakuwa et al. 2012):

$$T_{90} = (1 + z) \frac{E_{iso}}{L_{ave}}, \quad (7)$$

where isotropic energy E_{iso} is calculated with (Kakuwa et al. 2012):

$$E_{iso} = 10^{51.42 \pm 0.15} \text{erg} \left(\frac{E_p}{774.5 \text{keV}} \right)^{1.58 \pm 0.28}. \quad (8)$$

The average luminosity L_{ave} is calculated by $L_{ave} = 0.31L_p$.

3.6. Significance

Based on the preparations above, a group of GRBs can be constructed using Monte Carlo with the definite parameters ($\alpha, \beta, E_p, L_p, T_{90}, z$). Then the sample is ready for a quality check with Fermi-GBM observations. The significance for every GRB is calculated based on the expected signal and background number, N_{signal} and N_{bkg} . The signal can be obtained as

$$N_{signal} = \int_{E_{min}}^{E_{max}} N(E) T_{90} e^{-\tau(E,z)} A_{eff}^\gamma(E, \theta) dE, \quad (9)$$

where T_{90} is described in Equation. (7). $N(E)$ is the spectrum of the SGRB. A_{eff} is the effective area of the detector. For HADAR, the effective area is adopted from Ref. (Xin et al. 2021). The factor $e^{-\tau(E,z)}$ is from the EBL attenuation. The integral limit (E_{min}, E_{max}) is the detector's energy band, which is (10 GeV, 10 TeV) for HADAR.

For space-borne detectors such as GBM, N_{bkg} comes from cosmic γ background rates in the corresponding energy bands. For HADAR, N_{bkg} results from the cascades of cosmic rays:

$$N_{bkg} = \int_{E_{min}}^{E_{max}} S_p(E) T_{90} A_{eff}^p(E, \theta) \Omega(E) dE, \quad (10)$$

where $S_p(E)$ represents the spectrum of cosmic rays. A_{eff}^p is the effective area of HADAR corresponding to cosmic rays, and $\Omega(E)$ is the angular resolution of HADAR. These are given in Ref. (Xin et al. 2021).

A 5σ deviation is needed as a trigger, which is calculated as $N_{signal}/\sqrt{N_{bkg}} > 5$.

3.7. Check by Observations

The observation of Fermi-GBM is used to check our samples, and the detection rates of Fermi-GBM, Swift-BAT, and Fermi-LAT are used to check our detection

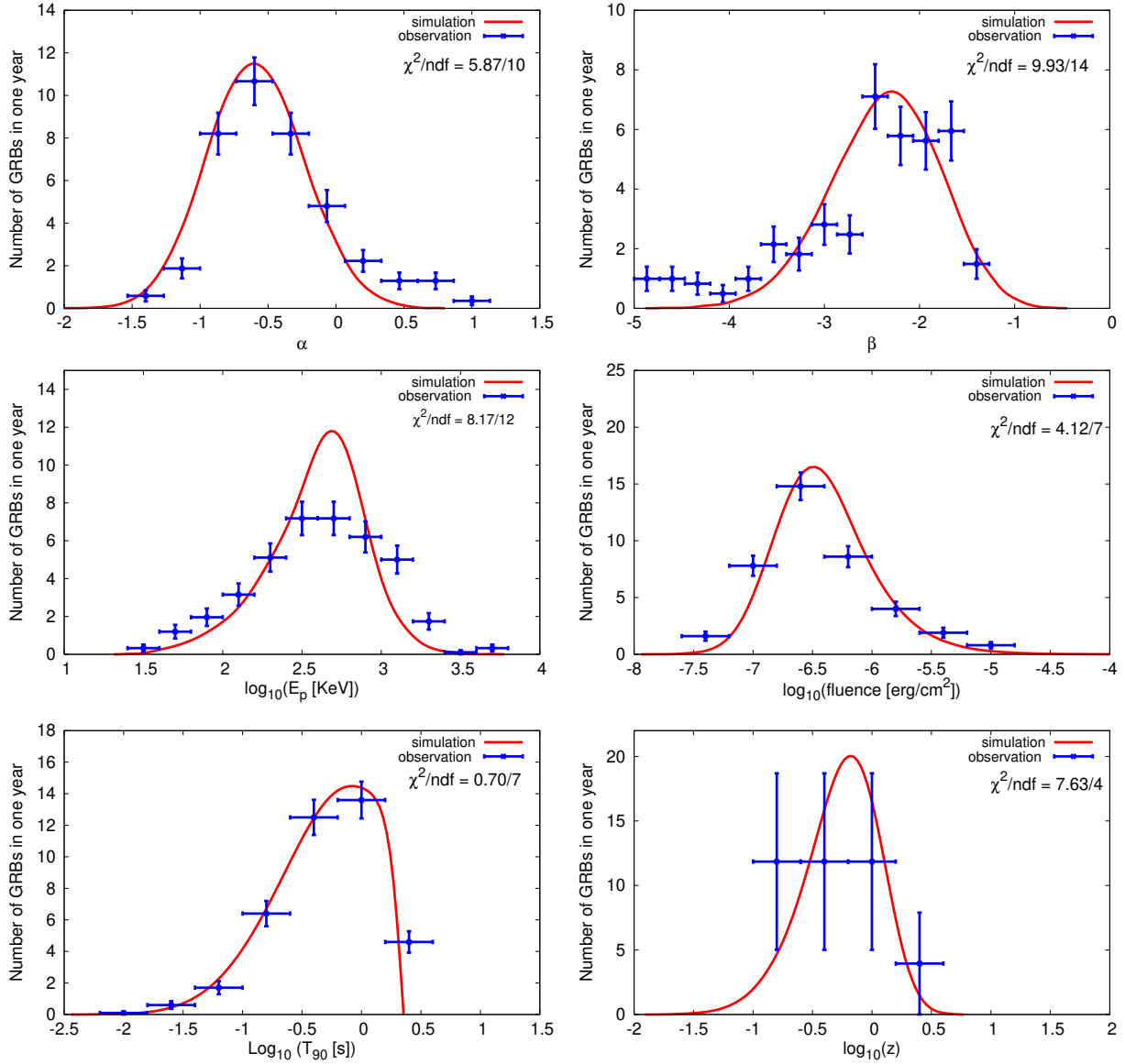


Fig. 3. Model results of α (top left), β (top right), E_p (middle left), flucence(middle right), T_{90} (bottom left), and redshift z (bottom right).

rate. In Fermi-GBM’s observational results, 395 SGRBs are observed in ten years. To evaluate the fitting quality, χ^2_{tot} is calculated as $\sum \chi_i^2 / \sum N_i^{bin}$, where i denotes $\alpha, \beta, E_p, z, T_{90}$, and the flucence, and N_i^{bin} is the corresponding bin number. The total combined χ^2_{tot} is 0.63.

The $\alpha, \beta, E_p, z, T_{90}$, and flucence distributions are compared between our phenomenological models and real observations, as shown in Figure 3. From Figure 3, it can be seen that our model results are roughly consistent with the real observations of Fermi-GBM given the experimental uncertainties.

Figure 4 shows the real detection rates of Fermi-GBM, Swift-BAT, and Fermi-LAT compared with our simulated detection rates. We find that at a low energy or

high energy, our simulated detection rates are roughly consistent with the real detection rates, given the experimental uncertainties.

4. RESULTS

The results of our work include two parts: the detected event rates of SGRBs, and a pseudo light curve for GRB090510 simulated with the HADAR experiment, which reflects HADAR’s capacity to detect VHE SGRBs with enough sensitivity and a wide FOV and to observe photons extending to the VHE spectral component.

4.1. Expected Detection Rates

The left panel of Figure 5 presents the expected detection rate between z and $z+dz$ for GBM and HADAR

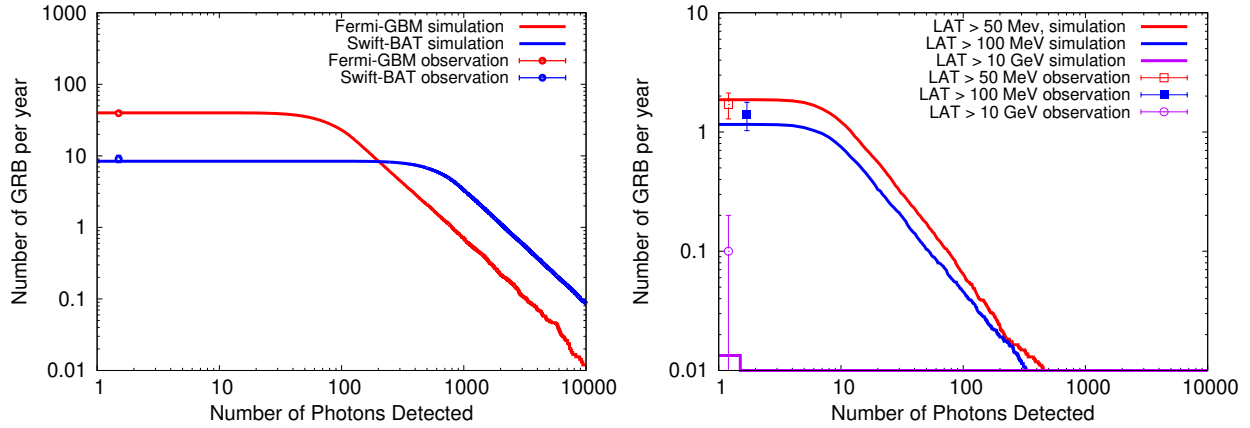


Fig. 4. The simulated detection rates of SGRB with Fermi GBM, Swift BAT, and Fermi LAT.

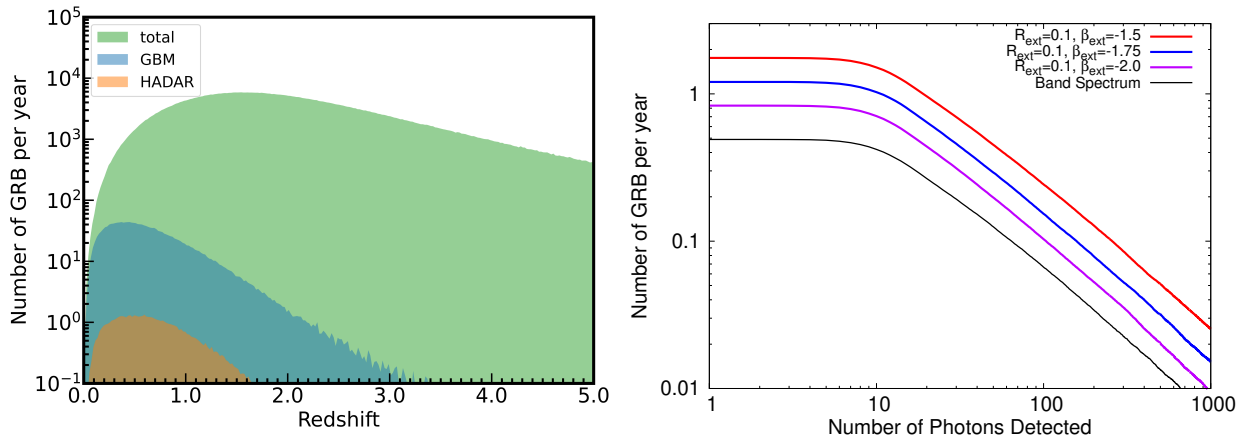


Fig. 5. Left: The SGRB detection rate between the redshift z and dz of GBM and HADAR is shown by the blue and orange lines, while the green line shows the BNS merger rate between the redshift z and dz . Right: The SGRB detection rate of HADAR for different combinations or parameters for the extra component, in which the black line and the cyan line represent the Band spectrum, the yellow, blue, and red lines represent the combination of the extra + Band components. The model of Ref. (Finke et al. 2010) is considered, and no internal absorption is taken into account.

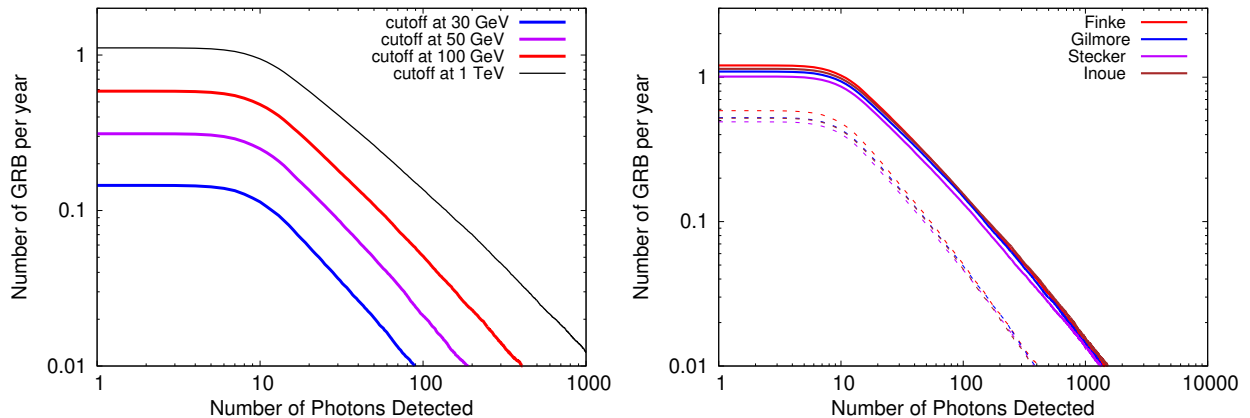


Fig. 6. Top left: The SGRB detection rate with the extra + Band spectra considered for different energy breaks, in the case of $\beta_{ext} = -1.5$, $R_{ext} = 0.1$, and the EBL model (Finke et al. 2010). Top right: The SGRB detection rate with the extra + Band spectra considered for different EBL models, $\beta_{ext} = -1.5$, $R_{ext} = 0.1$. The solid lines are cases without internal absorption and the dashed lines are the results when the energy spectrum is considered to cut off at 100 GeV.

compared with the BNS merger rate. The right panel

of Figure 5 presents the model calculation of the SGRB

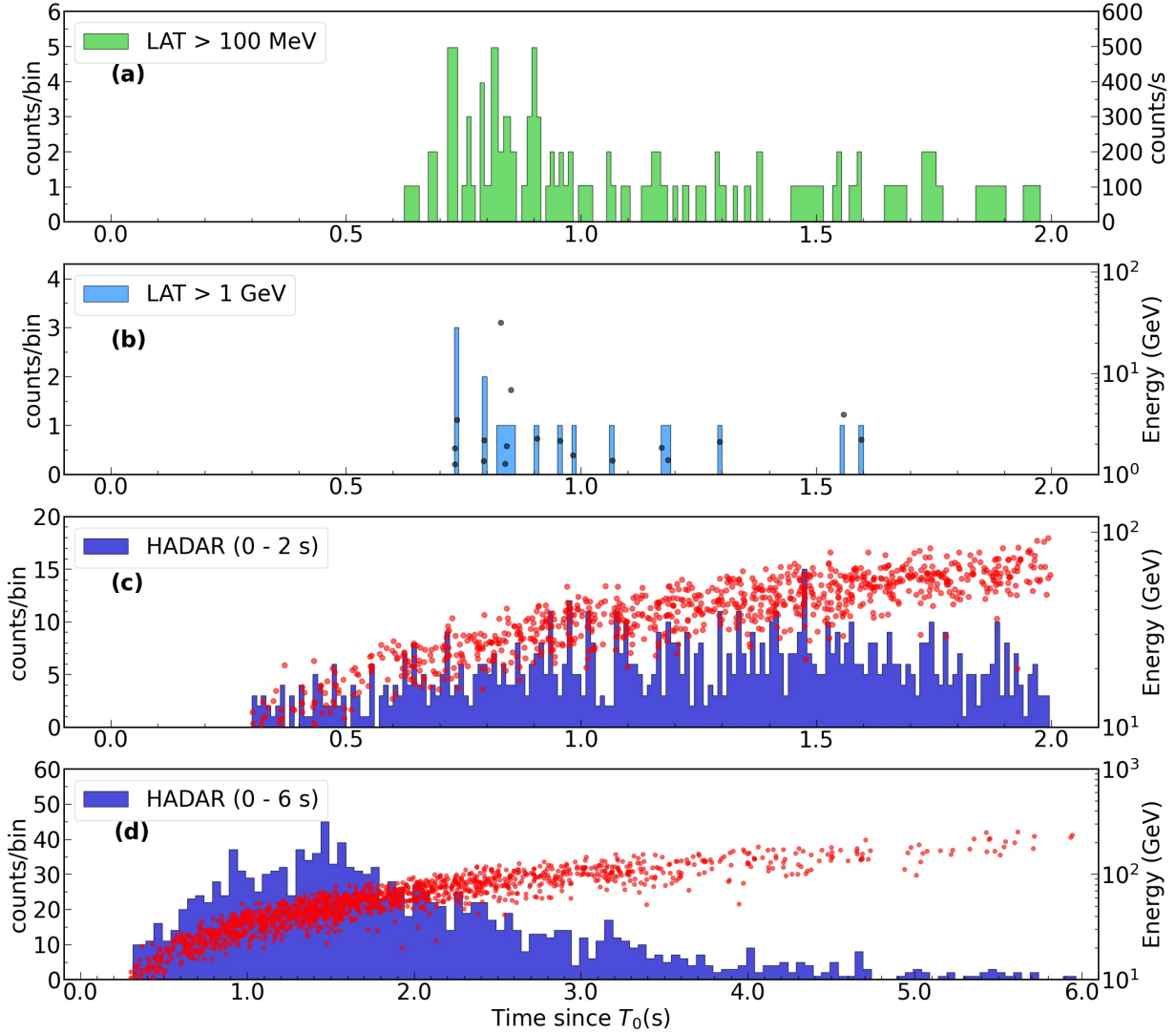


Fig. 7. Bottom: Light curves of GRB090510 at different energies. **a**, LAT light curve with $E < 100$ MeV. The per-second count rate is displayed on the right side for convenience. **b**, LAT light curve with $E < 1$ GeV. **c**, a simulated light curve of 090510-like GRB detected by HADAR. **b** and **c** also overlay the energy versus arrival time for each photon, with the energy scale displayed on the right side. **d**, the full light curve described in **c**. Photons are represented as gray and red dots in **b** and **c** separately.

detection rate for HADAR, which is the number of detected SGRBs as a function of the number of detected photons. The lines represent the extra spectra for the spectrum, $R_{ext} = 0.1$ and $\beta_{ext} = -2.0, -1.75, -1.5$. It is evident that the detection rate for HADAR is 0.49 per year for the Band spectrum. When the extra component with $R_{ext} = 0.1$ is considered, the detection rates for HADAR increase to 0.83, 1.2, and 1.8 for $\beta_{ext} = -2.0, -1.75, -1.5$.

Considering two-photon pair production within the emission region and during the propagation, the results are presented in Figure 6. It can be seen that the internal absorption prevents HADAR from observing the VHE photons to some extent. If the energy cutoff due to the two-photon pair production within the emission re-

gion is higher than 30 GeV, HADAR can detect at least 0.15 SGRB per year with the EBL model of Ref. (Finke et al. 2010). The result in the right-hand panel of Figure 6 shows that the different EBL models have a relatively small impact on the detection rate compared with that of the internal absorption. Adopting different EBL absorption models from Refs. (Finke et al. 2010; Gilmore et al. 2012; Stecker et al. 2012; Inoue et al. 2013), the expected detection rate of HADAR is approximately 0.49–1.1 SGRBs per year with or without a 100 GeV energy cutoff.

4.2. Pseudo Light Curve of GRB090510

Based on our HADAR model and the parameters of GRB090510 extracted from observational results (Ack-

ermann et al. 2010), including the redshift and spectrum, taking into account the model of the LIV effects for this GRB from Ref. (Abdo et al. 2009), a pseudo light curve of HADAR observation is generated, as shown in the lower panels (c) and (d) of Figure 7, as well as each photon with the observed time and energy.

To display this light curve, we consider the photon energy distribution to follow the spectrum of 090510-like GRB combined with EBL attenuation. Then, these photons are detected by HADAR with effective areas and a 20% energy resolution. An assumption is made that all photons from the source burst at exactly the same time, which means that the duration for the emission at the source is $\Delta t = 0$. For the LIV effects, a positive time delay $\Delta t = (\Delta E/E_{QG})D/c$ is included in the simulated arrival time of photons, where $E_{QG} = M_{QG}c^2$ is the Planck energy, D is the co-moving distance from source to detector, and $\Delta E = E_{\gamma,high} - E_{\gamma,low}$. The energy dispersion of the time delay $\Delta t/\Delta E = +0.03$ s/GeV is adopted (Abdo et al. 2009). From Figure 7, it is clear that HADAR works better in higher-energy photon detection than LAT, which is helpful for providing more constraints on the parameters of LIV effects.

5. CONCLUSIONS

The observations of TeV γ -ray emissions from SGRB are very important for studying the central engine, radiation mechanism, and the new physics of LIV particularly. Limited by the effective area and narrow FOV of space-borne and ground-based applications with IACT

technology experiments, there are still no results. The new experiments are required to have a wide FOV and high sensitivity with IACT technology. The HADAR experiment can fulfill these two characteristics simultaneously.

In this work, we produce one SGRB sample and then check the sample with Fermi-GRM, Fermi-LAT, and SWIFT observations. Based on this sample, the annual detection rate of SGRB is calculated for HADAR experiments. For the present status, the HADAR can detect 0.5 SGRB in one year. The annual rate can slightly change with different EBL absorption models and intrinsic spectral break-off. Furthermore, we assume that GRB090510A-like events appear in the FOV of HADAR. HADAR can detect about 2000 photons with the internal absorption considered. Simultaneously, the evolution effect of the light curve increases with the energy, which can be clearly observed when LIV happens in the Planck energy. Based on this work, we believe that the HADAR experiment has a good performance in the observation of SGRBs. We hope that the HADAR experiment will be successfully completed and that it can observe SGRBs that are consistent with our expectations in the future.

This work is supported by the National Natural Science Foundation of China (12263004, 12263005, and 12275279).

REFERENCES

- Abbott, B. P., Abbott, R., Abbott, T., et al. 2017, *The Astrophysical Journal Letters*, 848, L13
- Abdalla, H., Adam, R., Aharonian, F., et al. 2019, *Nature*, 575, 464
- Abdo, A., Ackermann, M., Ajello, M., et al. 2009, *Nature*, 462, 331
- Ackermann, M., Asano, K., Atwood, W., et al. 2010, *The Astrophysical Journal*, 716, 1178
- Ackermann, M., Ajello, M., Asano, K., et al. 2011, *The Astrophysical Journal*, 729, 114
- Aleksić, J., Ansoldi, S., Antonelli, L. A., et al. 2016, *Astroparticle Physics*, 72, 76
- Amelino-Camelia, G., Ellis, J., Mavromatos, N., Nanopoulos, D. V., & Sarkar, S. 1998, *Nature*, 393, 763
- Asano, K., & Inoue, S. 2007, *The Astrophysical Journal*, 671, 645
- Band, D., Matteson, J., Ford, L., et al. 1993, *The Astrophysical Journal*, 413, 281
- Band, D. L. 2003, *The Astrophysical Journal*, 588, 945
- Banerjee, B., Oganessian, G., Branchesi, M., et al. 2022, arXiv preprint arXiv:2212.14007
- Blinnikov, S., Novikov, I., Perevodchikova, T., & Polnarev, A. 1984, *Soviet Astronomy Letters*, 10, 177
- Bolmont, J., Corona, P., Gauron, P., et al. 2014, *Nuclear Instruments and Methods in Physics Research Section A: Accelerators, Spectrometers, Detectors and Associated Equipment*, 761, 46
- Chen, Y., Liu, R.-Y., & Wang, X.-Y. 2018, *Monthly Notices of the Royal Astronomical Society*, 478, 749
- collaboration, H., Abdalla, H., Aharonian, F., et al. 2021, *Science*, 372, 1081
- collaboration, L., et al. 2010, *Chinese Physics C*, 34, 249
- Dermer, C. D., Chiang, J., & Mitman, K. E. 2000, *The Astrophysical Journal*, 537, 785
- Eichler, D., Livio, M., Piran, T., & Schramm, D. N. 1989, *Nature*, 340, 126

- Finke, J. D., Razzaque, S., & Dermer, C. D. 2010, *The Astrophysical Journal*, 712, 238
- Ghisellini, G., Ghirlanda, G., Nava, L., & Celotti, A. 2010, *Monthly Notices of the Royal Astronomical Society*, 403, 926
- Gilmore, R. C., Somerville, R. S., Primack, J. R., & Domínguez, A. 2012, *Monthly Notices of the Royal Astronomical Society*, 422, 3189
- González, M., Rojas, D. A., Pratts, A., et al. 2023, *The Astrophysical Journal*, 944, 178
- Group, P. P. D. 2020, *Particle Physics Booklet*
- Howell, E., Ackley, K., Rowlinson, A., & Coward, D. 2019, *Monthly Notices of the Royal Astronomical Society*, 485, 1435
- Huang, Y., Hu, S., Chen, S., et al. 2022, *GRB Coordinates Network*, 32677, 1
- Inoue, Y., Inoue, S., Kobayashi, M. A., et al. 2013, *The Astrophysical Journal*, 768, 197
- Kakuwa, J., Murase, K., Toma, K., et al. 2012, *Monthly Notices of the Royal Astronomical Society*, 425, 514
- Kouveliotou, C., Meegan, C. A., Fishman, G. J., et al. 1993, *The Astrophysical Journal*, 413, L101
- leeds.ac.uk <http://www.cta-observatory.org>, C. C. J. K., Actis, M., Agnetta, G., et al. 2011, *Experimental Astronomy*, 32, 193
- MacFadyen, A., & Woosley, S. 1999, *The Astrophysical Journal*, 524, 262
- Madau, P., & Dickinson, M. 2014, *Annual Review of Astronomy and Astrophysics*, 52, 415
- Mészáros, P. 2006, *Reports on Progress in Physics*, 69, 2259
- Mészáros, P., & Rees, M. J. 1994, *Monthly Notices of the Royal Astronomical Society*, 269, L41
- Nakagawa, S., Takahashi, F., Yamada, M., & Yin, W. 2023, *Physics Letters B*, 137824
- Oganesyan, G., Nava, L., Ghirlanda, G., & Celotti, A. 2017, *The Astrophysical Journal*, 846, 137
- . 2018, *Astronomy & Astrophysics*, 616, A138
- Oganesyan, G., Nava, L., Ghirlanda, G., Melandri, A., & Celotti, A. 2019, *Astronomy & Astrophysics*, 628, A59
- Paczynski, B. 1986, *The Astrophysical Journal*, 308, L43
- Poolakkil, S., Preece, R., Fletcher, C., et al. 2021, *The Astrophysical Journal*, 913, 60
- Ravasio, M., Oganesyan, G., Ghirlanda, G., et al. 2018, *Astronomy & Astrophysics*, 613, A16
- Razzaque, S., Mészáros, P., & Zhang, B. 2004, *The Astrophysical Journal*, 613, 1072
- Regimbau, T., & Hughes, S. A. 2009, *Physical Review D*, 79, 062002
- Sari, R., & Esin, A. A. 2001, *The Astrophysical Journal*, 548, 787
- Stecker, F. W., Malkan, M. A., & Scully, S. T. 2012, *The Astrophysical Journal*, 761, 128
- Tsutsui, R., Yonetoku, D., Nakamura, T., Takahashi, K., & Morihara, Y. 2013, *Monthly Notices of the Royal Astronomical Society*, 431, 1398
- Veres, P., Bhat, P., Briggs, M., et al. 2019, *Nature*, 575, 459
- Wanderman, D., & Piran, T. 2015, *Monthly Notices of the Royal Astronomical Society*, 448, 3026
- Woosley, S. E. 1993, *The Astrophysical Journal*, 405, 273
- Xin, G.-G., Yao, Y.-H., Qian, X.-L., et al. 2021, *The Astrophysical Journal*, 923, 112
- Zhang, B. 2018, *The physics of gamma-ray bursts* (Cambridge University Press)
- Zhang, B., & Mészáros, P. 2001, *The Astrophysical Journal*, 559, 110